Near-field focusing by a photonic crystal concave mirror

Y. Saado, M. Golosovsky,[a] and D. Davidov
The Racah Institute of Physics, The Hebrew University of Jerusalem, Jerusalem 91904, Israel

A. Frenkel
ANAFA-Electromagnetic Solutions Ltd., P.O. Box 5301, Kiriat Bialik 27000, Israel

(Received 23 March 2005; accepted 7 August 2005; published online 29 September 2005)

We have studied the electric-field distribution in the photonic crystal (PC) concave mirror. This was done numerically and was verified in experiment. The field mapping in our experiments was performed using the Slater's perturbation technique which was modified for nonresonant structures. The PC consists of a planar array of dielectric rods with a trapezoidal depression that forms the concave mirror. At the midgap frequency of the first stopband of the underlying photonic crystal, the mirror allows focusing to a subwavelength spot size of $0.2\lambda \times 0.2\lambda$. The intensity is enhanced by 16 times at the focal point, as compared with the incident wave. © *2005 American Institute of Physics*. [DOI: 10.1063/1.2058179]

I. INTRODUCTION

The focusing of light using photonic band-gap materials is a subject of considerable interest. Photonic band-gap materials can be used to guide, focus, and localize electromagnetic waves. Several optical devices based on photonic band-gap materials, including waveguides, mirrors, and lasers, have been reported.[1–4] Photonic crystals can be also operated as "left handed materials" which are capable of focusing transmitted wave into a subwavelength spot due to the negative refraction.[5–8]

In this work we explore the possibility of focusing the electromagnetic radiation by a photonic band-gap material using a more "traditional way," namely, by a concave mirror made of an array of discrete scatterers. Focusing and imaging by the regular array of discrete scatterers is well known in the context of x-ray focusing by curved crystals[9,10] and Talbot self-imaging of periodic objects.[11,12] However, while the focusing in these cases is achieved due to the overlap of the far-field radiation of the scatterers, in the present case we discuss near-field focusing which can localize the light better than the far-field radiation can. Such focusing of light is similar to the one of electron scattering by optical corrals.[13,14]

The possible applications of this device should exploit field magnification rather than imaging and may include (i) coupling the energy in/out of the photonic crystals (in particular it can be used as antenna feed), and (ii) impedance matching. Although such elements may be fabricated using conventional technologies using metallic or dielectric mirrors, there are certain advantages in using photonic crystal matrix. Indeed, to make functional devices from photonic crystals one would like to fabricate all components using the same technology. For example, to couple energy in/out of planar photonic crystal (PC) the lenses and mirrors should be better fabricated from the same building blocks of PC.

In the present work we demonstrate a focusing mirror fabricated from the photonic crystal and operating in the microwave range. We believe that once the experimental proof of concept for such a near-field focusing is achieved, our design is scalable to the optical range. While our experiments were performed with the photonic crystal made of $\epsilon=90$ dielectric rods, we made extensive computer simulations for the PC concave mirrors made from the dielectric rods with lower dielectric constants $\epsilon=12.9$ and $\epsilon=9.7$ and found that these devices also demonstrate focusing. By optimizing the frequency, rod diameter, and spacing between the rods we achieved a field magnification in the focus of up to 9. Therefore, we believe that our results are indeed scalable to the optical frequencies.

II. EXPERIMENT

A. Photonic crystal

Our PC consists of cylindrical rods of 2.5 mm diameter and 10 mm height, made from a low-loss microwave ceramics with dielectric constant $\epsilon=90$.[15] The rods are mounted in the hexagonal array of holes made in the light-weight matrix with the dielectric constant 1.1 [Fig. 1(a)]. The distance between the rods is $d=5.4$ mm and the corresponding lattice constant is $a_L=d\sqrt{3}/2=4.7$ mm. The array consists of 22 rows, with 10 rods in each row. Several rods from the front rows of the array were removed to achieve a trapezoidal depression which, as we will show further, operates as a focusing mirror. This array is mounted in the rectangular waveguide with a removable cover plate. The rods in the two rows adjacent to the waveguide sidewalls were cut in two halves to imitate periodic boundary conditions at the ideally conducting wall. In such a way our measurements could be generalized to an infinitely wide array.

The main reason for using a waveguide rather than a free-space propagation[18] is to force the incident wave to propagate through a photonic crystal, in other words, to eliminate diffraction losses. To accommodate the photonic crystal of sufficient width, we used a homemade rectangular waveguide with dimensions $a=54$ mm and $b=10$ mm and the cutoff frequency of 2.8 GHz. To launch the wave into the

[a]Electronic mail: golos@vms.huji.ac.il

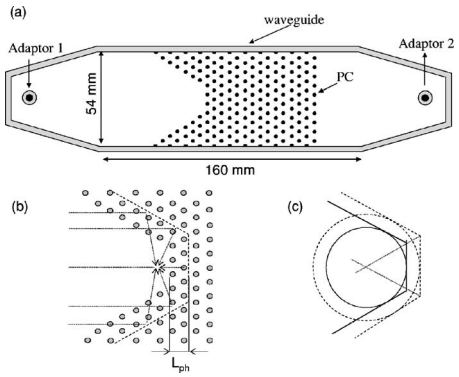

FIG. 1. (a) Design of the measurement setup (top view image, in scale). A hexagonally ordered array of dielectric rods is mounted inside a rectangular metallic waveguide. The front surface of the array has a trapezoidal depression which mimics a concave mirror. The waveguide cover plate is not shown here. (b) Schematic drawing of the focusing by a concave photonic crystal mirror. Open circles represent dielectric rods. Reflection from the PC may be described as a reflection from the virtual high-impedance planes located at the distance L_{ph} inside the crystal (dashed lines). The focal point of this surface is shown by the star. (c) Schematic drawing illustrating an effective curvature of the mirror.

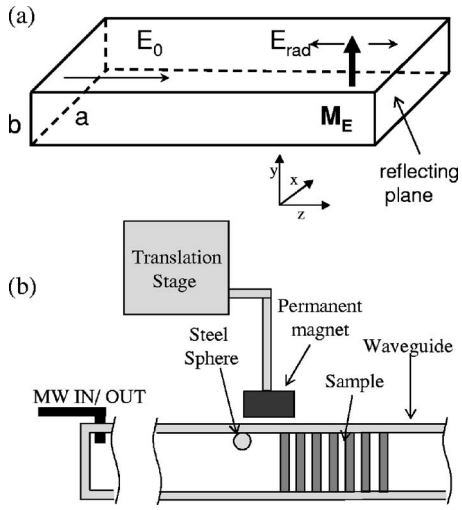

FIG. 2. (a) Schematic drawing showing the perturbation technique. A polarizable object is situated inside the rectangular waveguide at the distance z from the partially reflecting plane. The electric field in the waveguide induces in this object a dipole moment which radiates back and forth. (b) Experimental realization of the perturbation technique. A small steel sphere is remotely moved inside the waveguide using a permanent magnet attached to the translation stage. The reflected wave carries information on the electric field at the position of the sphere.

waveguide we designed special coax-to-waveguide adaptors operating in the frequency range of 4–11 GHz.

To achieve optimal design of the waveguide, adaptor, and the array of rods we used computer simulations (ANSOFT HFSS, CST Microwave Studio Solver). We aimed at using the rods with high dielectric constant $\epsilon \sim 90$, and at the first step we found the optimal radius of these rods, the lattice constant of the array, and the width and height of the waveguide. Our purpose was to fit the first stop band of our photonic crystal to the frequency range of the waveguide-adaptor assembly. At the second step we found the optimal shape of the trapezoidal depression at the front surface of the array in order to achieve the most effective field concentration at the focus [Fig. 1(b)]. This was done for the frequency corresponding to the midgap of the first stop band. At the third step we built the setup accordingly and mapped the electric field distribution there. In such a way we verified the focusing performance of our concave mirror.

B. Perturbation technique - the model

To map the field distribution in the waveguide we choose a scanning perturbation technique.[16–19] This technique uses a small object which perturbs the microwave field and is remotely moved inside the microwave device. By comparing device performances when the perturbing object is situated at different locations, one can map the field distribution there. In the past this technique was used to map the field distribution in two-dimensional microwave *resonators* by detecting resonant frequency shifts introduced by a small conducting sphere. In our present work we use the similar approach to map the field distribution in the *nonresonant* waveguiding structure. This is done by the phase-sensitive measurement of the radiation scattered by a small sphere at different locations in the waveguide.

The theoretical framework of our technique follows Slater's[16] derivation of the radiation of the electric dipole in the rectangular waveguide. We assume an air-filled rectangular TE_{10} waveguide terminated by the matched load, a dominant TE_{10} mode excited there, and a small polarizable object with the electric susceptibility α_E situated inside the waveguide [Fig. 2(a)]. The electric field of the TE mode induces in this object an electric dipole moment which is directly proportional to the electric field at its position, i.e.,

$$M_E = \alpha_E E(x,y,z). \tag{1}$$

Although this induced dipole radiates in all directions, the boundary conditions imposed by the waveguide walls allow only backward and forward propagating waveguide modes. In particular, the magnitude of the TE_{10} mode radiated by the dipole is[16]

$$E_{\mathrm{rad}} = \frac{\omega Z \alpha_E E_y(x,z)}{ab} \sin\frac{\pi x}{a}. \tag{2}$$

Here $Z = Z_0/\sqrt{1-[\pi/(ka)]^2}$ is the TE-mode impedance, Z_0 is the impedance of free space, k is the wave vector in free space, a,b are the long and short dimensions of the waveguide, and $E_y(x,z)$ is the y component of the microwave electric field at the object location (x and z components of M_E do not radiate into the TE_{n0} mode). It can be also shown[16] that the radiated field [Eq. (2)] does not depend on the distance between the electric dipole and the broad waveguide wall, y. By launching the TE_{10} mode into the waveguide and by measuring the reflected wave at different positions of the object we can map the electric-field distribution in the waveguide $E_y(x,z)$ using Eq. (2). The magnetic-field distribution can be measured in a similar way using a small magnetizable object.

For the waveguide loaded with an unmatched load, Eq. (2) is modified. In this case the reflected wave consists of three contributions: (i) reflection from the load, (ii) backscattering from the object [Eq. (2)], and (iii) reflection at the unmatched load of the forward scattered wave from the object. Only the two last contributions depend on the location of the perturbing object. They can be considered as a coherent sum of the radiation of the dipole and the radiation of the image dipole. The interference between these two terms results in the additional complex factor $A=e^{-j\beta z}+\Gamma e^{j\beta z}$ that shall be introduced into Eq. (2). Here, $\Gamma=re^{j\Phi}$ is the complex reflection coefficient of the load, $\beta=[k^2-(\pi/a)^2]^{1/2}$ is the propagation constant in the waveguide, and z is the distance between the dipole and the reflecting plane [Fig. 2(a)]. Equation (2) now reads

$$E_{\mathrm{rad}}(x,z)=A(z)\frac{\omega Z\alpha_E E_y(x,z)}{ab}\sin\frac{\pi x}{a}. \tag{3}$$

For example, if the load is an ideal conducting mirror ("short"), $\Gamma=-1$, $A=2\cos\beta z$, and the electric field in the waveguide is $E(x,y,z)=E_0\sin(\pi x/a)\cos\beta z$. Here, E_0 is the electric-field magnitude in the incident wave. Then, Eq. (3) yields

$$E_{\mathrm{rad}}=\frac{4\omega Z\alpha_E E_0}{ab}\sin^2\frac{\pi x}{a}\cos^2\beta z. \tag{4}$$

C. Perturbation technique - the implementation

As a perturbing object we used a small steel sphere with the radius $R=1$ or 1.5 mm. This sphere is sufficiently small to minimally perturb the field in the waveguide. It can be considered ideally conducting, since the skin depth at microwave frequencies is much smaller than the radius of the sphere. The electric susceptibility of an ideally conducting sphere is $\alpha_E=4\pi\epsilon_0R^3$. When this sphere is mounted in the rectangular waveguide where the *TE* mode is excited, it acquires an electric dipole moment, oriented perpendicularly to the broad wall of the waveguide, and radiates. This radiation is different from the dipole radiation in free space, since it includes a radiation of the image dipoles which interfere *constructively* with the radiation of the primary electric dipole.

It should be noted that the ideally conducting sphere has also a magnetic susceptibility, $\alpha_H=-2\pi\epsilon_0R^3$, therefore the microwave magnetic field of the *TE* mode induces there a magnetic moment as well. This moment is *parallel* to the broad waveguide wall. However, for the conducting sphere in the vicinity of the broad wall of the rectangular waveguide, the magnetic dipole radiation is negligible due to the *destructive* interference with the radiation of the image dipole. Therefore, the field scattered by the conducting sphere in the close vicinity to the broad waveguide wall is mostly determined by the microwave electric field.

The electric-field mapping in the waveguide was performed as follows. We launched the microwave with a known magnitude E_0 and frequency ω into the waveguide [Fig. 2(b)]. Then we measured the magnitude and phase of the reflectivity S_{11} while moving the conducting sphere inside the waveguide. This was done with the HP-8510C vector network analyzer. The motion of the sphere was performed using a permanent rare-earth magnet mounted on the positional stage [Fig. 2(b)]. We subtracted the reflectivity without the sphere from the obtained results and found $\Delta S_{11}(x,z)\sim E_{\mathrm{rad}}/E_0$. Here, (x,z) is the position of the sphere, E_0 is the field in the incident wave, and E_{rad} is given by Eq. (3).

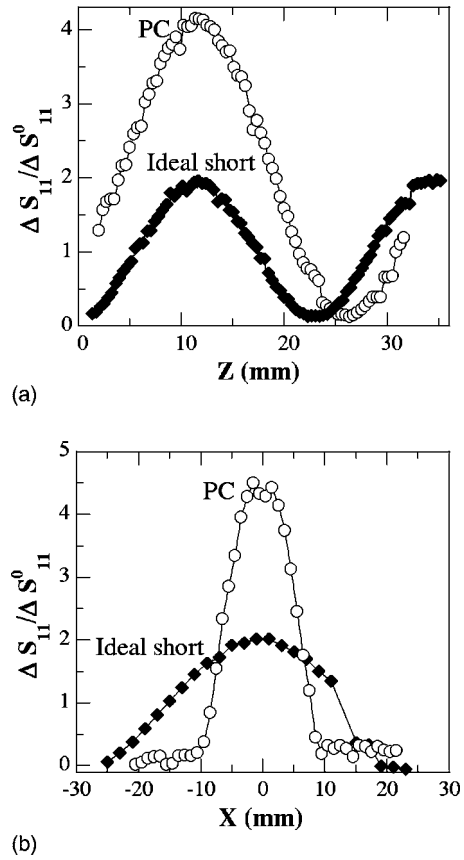

FIG. 3. Electric field magnitude in different directions with respect to the direction of propagation: (a) longitudinal and (b) transverse. Filled symbols show the field magnitude in front of the photonic crystal shown in Fig. 1. The measurements have been performed with a perturbation technique using a 2-mm-diameter steel sphere. The frequency 7 GHz is in the midgap of the first stopband. $z=0$ plane corresponds to the front surface of the innermost row of rods (see Fig. 1). Open symbols show the results for the flat conducting mirror at $z=0$ and at 7 GHz. The lines are the guides to the eye. Note the sharp peak in (b) indicative of focusing.

To verify the technique we mapped the two-dimensional field distribution in front of the flat metallic mirror (ideal short). In the z direction we obtained the well-known standing wave pattern in the waveguide [Fig. 3(a)], as predicted by Eq. (4). The field magnitude in the x direction, the frequency dependence, and the magnitude of ΔS_{11} are also well accounted for by Eq. (4).

The application of this technique to the photonic crystal is not straightforward. Note that Eq. (3) allows the determination of $E_y(x,z)$ for known x,z. In the case of the photonic crystal, which represents the distributed load, this procedure is somewhat complicated since the position of the reflecting plane is not known in advance. Therefore, in our mapping of the field distribution upon reflection from the photonic crystal we plot $|E_{\mathrm{rad}}(x,z)|$ as given by Eq. (3).

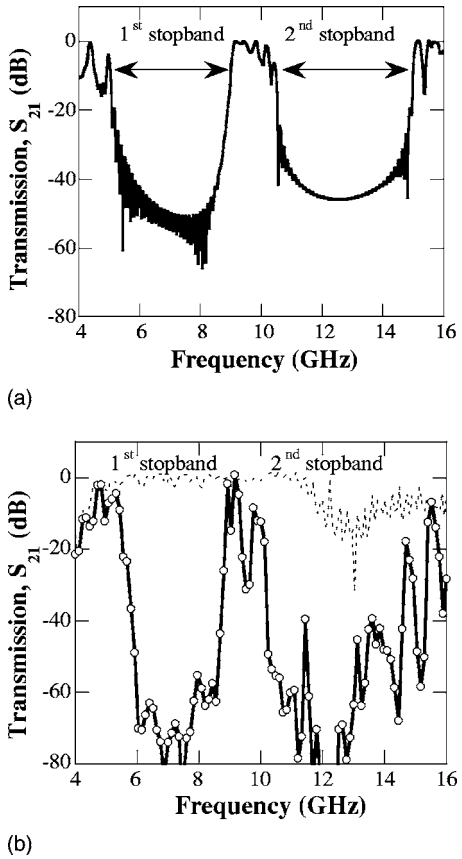

FIG. 4. Microwave transmission through our device. (a) Computer simulations using CST MICROWAVE STUDIO software. The simulations assume six rows of the hexagonally packed rods in the conducting rectangular waveguide. (b) Experimental results (ten rows). The dotted line corresponds to the transmission measurement in the empty waveguide. Note good correspondence between the experiment results and the model.

III. EXPERIMENTAL RESULTS

A. Microwave transmission through the photonic crystal

Figure 4(a) shows a numerical simulation for the microwave transmission through the array consisting of six full rows of dielectric rods in the waveguide. The simulation predicts the first stop band at 5.4–8.9 GHz and the second stop band at 10.2–14.6 GHz. Figure 4(b) shows corresponding experimental results (for the ten-row array). The experimental data agree well with the numerical simulation. We clearly observe the first stop band and the low-frequency edge of the second stop band. We also observe a narrow band at 9.7 GHz which is absent in numerical simulations. The depth of the first stop band in our experiments (70 dB) exceeds that in simulations (50 dB) since our experimental array contains more crystalline rows.

B. Field mapping in one dimension

We performed field mapping upon reflection from our device using the perturbation technique at the midgap frequency of 7 GHz. Figure 3(a) shows our results for the direction along the symmetry plane, while Fig. 3(b) shows corresponding results for the transverse direction. In the longitudinal direction we observe a strong maximum in the close proximity to the array of rods and several weak maxima further away [Fig. 3(a), open symbols]. This strong maximum indicates on focusing, while the weak maxima are simply standing waves. (Their spatial periodicity is $\lambda/2$; hence the Talbot effect[12] is excluded). In comparison, we show field mapping results achieved upon reflection from the flat conducting mirror [Fig. 3(a), filled symbols]. Here we also observe several maxima. However, these maxima arise from the well-known standing wave, rather than from focusing. The field magnitude in the standing wave maximum is twice as big as that in the incident wave. However, the magnitude of the maximum corresponding to the reflection from our photonic device exceeds by 4–5 times the field of the incident wave. In the transverse direction we observe a sharp peak corresponding to our device as compared with the wide peak corresponding to the standing wave in the waveguide.

To verify our results shown in Fig. 3, we repeated these measurements using the conventional slotted-line technique. It employs a small antenna which is scanned along a narrow slot in the broad waveguide wall and picks up the electric field there. (Unfortunately, this technique is not suitable for the two-dimensional field mapping). The slotted-line measurements yield three- and four-fold field amplifications in the focus which is consistent with our perturbation technique measurements.

C. Two-dimensional measurements

To study the spatial extent of the field maximum in the focus (Fig. 3) we performed two-dimensional field mapping using a perturbation technique. Figure 5(a) shows results of computer simulations of the electric-field magnitude in front of our device, and Fig. 5(b) shows corresponding experimental results. Note that there is a good qualitative correspondence between the experimental results and numerical simulations. We observe a sharp maximum indicating focusing in both longitudinal and lateral directions.

D. Focusing at different frequencies

We performed two-dimensional field mapping (Fig. 5) for different frequencies, corresponding to the stopband and passband as well. For the frequencies inside the stopband we observe a sharp maximum with pronounced magnitude, indicative of focusing, while for the frequencies in the passband, the maximum is broad and weak. To quantitatively characterize the size of the maximum we approximate the field in its vicinity by the Gaussian

$$\Delta S_{11}(x,z) \propto E_y(x,z) \propto \exp - \left[\frac{(x-x_0)^2}{w^2} + \frac{(z-z_0)^2}{d_f^2} \right]^2, \quad (5)$$

where w and d_f are the lateral and longitudinal sizes of the focusing spot, respectively.

Figure 6 shows $z_{\max}$ (focal length) as measured from the front surface of the mirror. We observe linear dependence on wavelength, $z_{\max} \sim 0.52\lambda$ in the stopband. The lateral and longitudinal sizes of focus also linearly depend on wavelength, $w \sim 0.17\lambda$ (Fig. 6, open symbols) and $d_f \sim 0.17\lambda$ (Fig. 7). Note that in our experiments we find ΔS_{11} as given by Eq. (3) and take it as a measure of the field $E_y(x,z)$; i.e., we

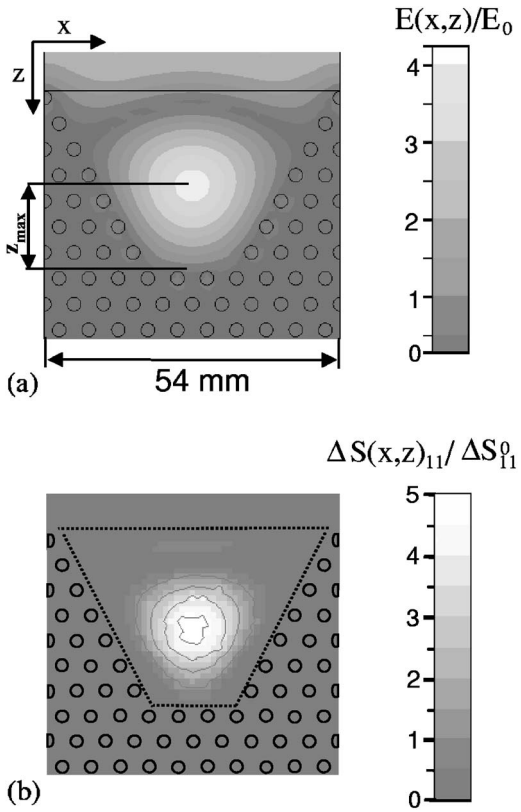

FIG. 5. Two-dimensional field distribution in the *XZ* plane, and at 7 GHz. The device is the concave photonic crystal shown in Fig. 1. (a) Computer simulations using CST Microwave Studio. z_{max} shows the position of the focus. (b) Experimental results by the perturbation technique using a 2-mm-diameter steel sphere. The dashed line in (b) shows the area in which we performed field mapping.

replace $A(z)$ by 2 and $\sin \pi x/a$ by 1. In such a way the size of the focal spot is underestimated, although the error is not significant. For example, taking into account the $\sin \pi x/a$ factor in Eq. (3) we find the actual spot size of $w = 0.18-0.19\lambda$ instead of $w=0.17\lambda$.

To measure the field magnitude in the focus we performed a one-dimensional scanning along the symmetry plane of the waveguide and measured the reflectivity at different frequencies. Here we met with two complicating factors. One of them is multiple reflections occurring when our radiating dipole is located in front of a curved reflecting surface. The waves reflected from different parts of this surface and from the waveguide sidewalls interfere. This interference is strongly frequency dependent, in such a way that the backscattered radiation due to the dipole is modulated in the frequency domain. To get rid of this modulation, we performed vector reflection measurements in the wide frequency range at each location of the sphere (along the symmetry plane of the waveguide), converted the results from the frequency domain to the time domain, performed temporal filtering which eliminates multiple reflections, and got back to the frequency domain. Another complication is that our launcher-waveguide assembly is designed to operate below 11 GHz [see Fig. 4(b), dashed line], while we are willing to achieve some limited information from the experimental results above 11 GHz as well. It seems that in the second stopband, which appears above 11 GHz, we also observe focusing.

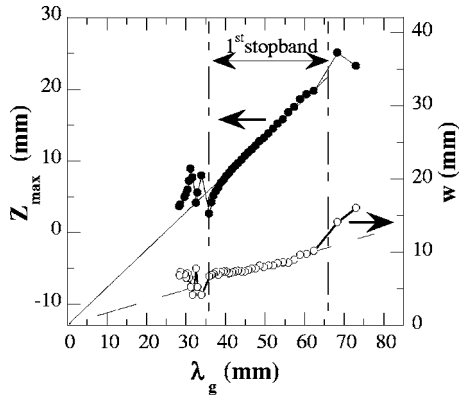

FIG. 6. Filled symbols show location of the maximum z_{max} as a function of the wavelength in the waveguide $\lambda_g=\lambda/\sqrt{1-[\pi/(ka)]^2}$. $z=0$ corresponds to the outer surface of the innermost row of rods (Fig. 1). The solid line shows linear approximation $z_{max}=0.53\lambda+z_1$ where $z_1=12$ mm. Open symbols show the size of the focusing spot w in the lateral direction. The dashed line shows linear approximation $w=0.17\lambda$.

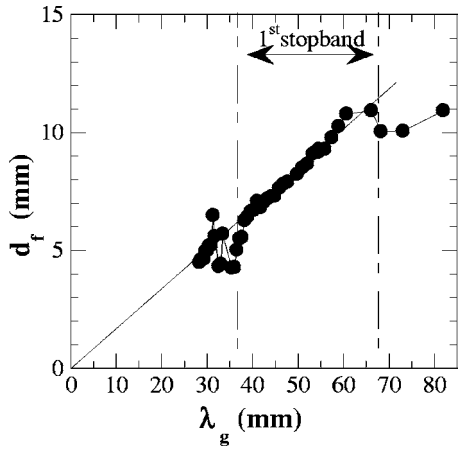

FIG. 7. The size of the focusing spot d_f in the longitudinal direction as a function of the wavelength in the waveguide λ_g. The solid line shows linear approximation $d_f=0.17\lambda$.

We found the field maximum in the focus and determined its position, z_{max}. The field magnification at the maximum, $M=E(z_{max})/E_0$, as given by Eq. (3), is $M \propto \Delta S_{11}/A\omega$. As we will show in the next section, the focusing maximum occurs exactly at the standing wave maximum, where A achieves its maximum value $A=2$. Figure 8 shows $\Delta S_{11}/\omega$ as a function of frequency. The magnification is maximum in the stopband and shows a trend to higher M with increasing frequency. Focusing in the passband is insignificant.

IV. DISCUSSION

Our device can be considered as a resonant cavity with a wide coupling aperture, whereas the focal spot corresponds to the electric field antinode. The device also loosely reminds one of a parabolic dish antenna fabricated from photonic crystal. We attribute the focusing effect found in our studies as arising from the standing wave in the direction of propagation, which is additionally amplified by the standing wave in the lateral direction arising from the concave surface of the reflecting array. To find where the focusing occurs, we need to recall the phase properties of photonic band-gap ma-

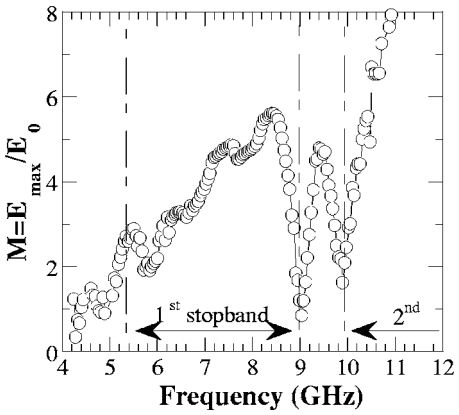

FIG. 8. Field magnitude at the focus (open symbols) as compared to the field in the incident wave. $M=1$ corresponds to the traveling wave; $M=2$ corresponds to the standing wave in the waveguide terminated by the ideal short. The continuous line shows frequency dependence of the transmission through the device. Note the similarity between these two dependences. Here, the measurements were performed using a 3-mm-diameter steel sphere.

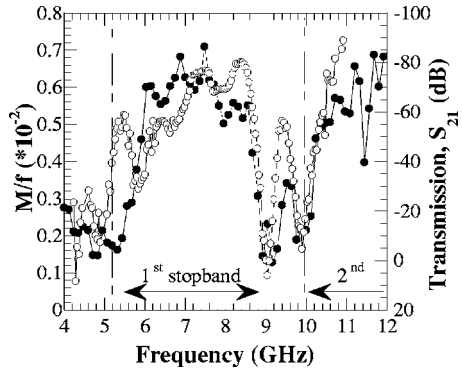

FIG. 9. Open symbols show a frequency dependence of M/f from Fig. 8. Here, f is the microwave frequency and M is defined in Fig. 8. Filled symbols show $-\ln T$ (S_{12} in the logarithmic scale). Note the similarity between these two curves.

terials. As we have shown elsewhere,[20] the phase of the wave reflected from the photonic crystal is strongly frequency dependent:

$$\Phi(k) \simeq \Phi(k_0) + \frac{\partial \Phi}{\partial k}(k - k_0). \tag{6}$$

Here k_0 is the wave vector corresponding to the midgap and $\Phi(k_0)$ is the phase shift at the midgap frequency. It can be shown that $\Phi(k_0)=n\pi$ where $n=0$ or 1.[20] Equation (6) can be recast in a different form:

$$\Phi(k) \simeq \Phi_0 + 2kL_{\mathrm{ph}}, \tag{7}$$

where $L_{\mathrm{ph}}=\partial\Phi/2\partial k$ is the so-called phase penetration length and

$$\Phi_0 = \Phi(k_0) - 2L_{\mathrm{ph}}k_0. \tag{8}$$

Equation (8) means that the reflection from the photonic crystal looks as if it were occurring from the virtual plane located at the distance L_{ph} from the front surface of the photonic crystal [Fig. 1(b)], whereas the phase shift upon reflection from this virtual plane is Φ_0. The phase penetration length is closely related (but not necessarily equal) to the localization length $L_{\mathrm{loc}}=-(d\ln T/dt)^{-1}$ where T is the transmission through photonic crystal and t is its thickness. The L_{ph} is almost constant at the midgap and sharply increases at the gap edges.

We relate the focusing maximum observed in our experiments with a concave photonic crystal mirror to the first standing wave maximum upon reflection from it. Indeed, the first standing wave maximum occurs at the distance $z_{\max}$ (measured from the front surface of the photonic crystal) found from the condition

$$2kz_{\max} + \Phi(k) = 2\pi. \tag{9}$$

We substitute here $\Phi(k)$ from Eq. (7) and find the following using Eq. (8)

$$z_{\max} = \frac{\lambda}{2}\left[1 - \frac{\Phi(k_0)}{2\pi}\right] + L_{\mathrm{ph}}\left(\frac{\lambda}{\lambda_0} - 1\right). \tag{10}$$

Here λ_0 is the wavelength corresponding to the midgap frequency. At this frequency, Eq. (10) yields $z_{\max}=\lambda_0/2$ for $\Phi(k_0)=0$, and $z_{\max}=\lambda_0/4$ for $\Phi(k_0)=\pi$.

Our experimental results for the position of the maximum $z_{\max}$ (Fig. 6) are consistent with these predictions. Indeed, we observe a linear dependence of $z_{\max}$ on wavelength, which is consistent with Eq. (10). The focal position at midgap frequency of 7 GHz is $z_{\max}=12$ mm which is very close to $\lambda_0/4=11.2$ mm.

At the next step we found L_{ph} from our experimental data. As suggested by Eq. (10), L_{ph} can be found as an intercept of linear dependence $z_{\max}(\lambda)$ with the vertical axis. Figure 6 yields $L_{\mathrm{ph}}=13$ mm at the midgap. This corresponds to a very small phase shift at the midgap [Eq. (6)], $\Phi_0=-0.067\pi$, and means that with respect to reflection, our photonic crystal can be replaced by a virtual *high-impedance* plane which is situated at the distance $L_{\mathrm{ph}}=12$ mm inside the crystal, as it is shown by dashed lines in Fig. 1(b). The focusing here arises from the standing wave maximum in the z direction which is additionally amplified by the standing wave in the perpendicular x direction. Since this maximum arises from interference, it is quite natural to assume that its size scales with the wavelength. Indeed, Figs. 6 and 7 show that the lateral size w and the longitudinal size d_f of the focusing maximum linearly depend on wavelength (of course, this pertains only to the frequencies in the stopband).

The magnification can be explained along the similar lines. Indeed, our concave photonic mirror can be approximated by a cylindrical high-impedance surface with the curvature radius $R_{\mathrm{cyl}}=R_0+L_{\mathrm{ph}}$, where R_0 is the effective curvature radius of the front surface of the photonic crystal [Fig. 1(c)]. The field magnification in the focus of a cylindrical mirror is $M\sim D/\lambda F$, where D is the aperture size and $F=R_{\mathrm{cyl}}/2D$ is the F number. Therefore, for a conventional cylindrical mirror, $M\propto 1/\lambda\propto f$, where f is the frequency. For a photonic crystal mirror, the situation is more complicated since the effective curvature radius R includes L_{ph} which is frequency dependent. Its frequency dependence can be crudely estimated from the following considerations. The

phase penetration length is closely related to the localization length, $L_{ph} \sim L_{loc} \propto -1/\ln T(f)$. Here T is the transmission through the crystal. Therefore, $L_{ph}=$const in the midgap and sharply increases at the gap edges. Its frequency dependence closely follows that of transmission. Therefore, we expect that $M \propto -(\ln T)/\lambda$, in other words, $M/f \propto -\ln T$. Indeed, Fig. 9 shows that the frequency dependence of M/f mimics the frequency dependence of $-\ln T$.

V. CONCLUSIONS

We demonstrate a photonic crystal mirror that exhibits focusing for the frequencies corresponding to the stopband. At the midgap frequency of the first stop band it showed the 16-fold power enhancement in the focus. The frequency dependence of magnification closely follows the localization length while the focal position linearly depends on wavelength inside the stopband.

Comparing the present method with other subwavelength focusing techniques, such as the Fresnel plate[21] or the slab made of a left-handed material,[5] we emphasize that the focusing of our concave PC mirror arises both from the properties of the photonic crystal and from the shape of the mirror.

ACKNOWLEDGMENTS

This work was supported by the Israeli Science Foundation and by the Israeli Ministry of Science and Technology. We are grateful to F. Sakran, A. Copty, and Y. Neve-Oz for experimental assistance.

[1] M. M. Beaky, J. B. Burk, O. Everitt, M. A. Haider, and S. Venakides, IEEE Trans. Microwave Theory Tech. **47**, 2085 (1999).
[2] M. Loncar and A. Scherer, Appl. Phys. Lett. **82**, 4648 (2003).
[3] S. Enoch, G. Tayeb, and B. Gralak, IEEE Trans. Antennas Propag. **50**, 2089 (2003).
[4] E. Ozbay, I. Bulu, K. Aydin, H. Caglyas, K. B. Alici, and K. Euven, Laser Phys. **15**, 217 (2005).
[5] J. B. Pendry, Phys. Rev. Lett. **85**, 18 (2000).
[6] P. Markos and C. M. Soukoulis, Phys. Status Solidi A **197**, 595 (2003).
[7] S. Foteinopoulou, E. N. Economou, and C. M. Soukoulis, Phys. Rev. Lett. **90**, 107402 (2003).
[8] P. V. Parimi, W. T. Lu, P. Vodo, and S. Sridhar, Nature (London) **426**, 426 (2003).
[9] F. N. Chukhovskii, W. Z. Chang, and E. Foerster, J. Appl. Phys. **77**, 1843 (1995).
[10] W. Z. Chang and E. Foerster, J. Opt. Soc. Am. A **14**, 1647 (1997).
[11] C. Wang, J. Azuna, and L. R. Chen, Opt. Lett. **29**, 1590 (2004).
[12] J. M. Tobias and H. Grebel, Opt. Lett. **24**, 1660 (1999).
[13] C. Chicanne *et al.*, Phys. Rev. Lett. **88**, 097402 (2002).
[14] M. F. Crommie, C. P. Lutz, and D. M. Eigler, Science **262**, 218 (1993).
[15] Ceramic dielectrics, Model No. T90A, HILTEK MICROWVE LTD, Newton House Winch Road (Sittingboum Research Center) Kent ME9 8EF, UK.
[16] J. C. Slater, *Microwave Transmission* (Dover, New York, 1959), p. 280.
[17] L. C. Mair, J. R. Terrall, and J. C. Slater, J. Appl. Phys. **23**, 68 (1952).
[18] S. Sridhar, Phys. Rev. Lett. **67**, 785 (1991).
[19] A. Gokirmak, D. H. Wu, J. S. A. Bridgewater, and S. M. Anlage, Rev. Sci. Instrum. **69**, 3410 (1998).
[20] M. Golosovsky, Y. Neve-Oz, D. Davidov, and A. Frenkel, Phys. Rev. B **70**, 115105 (2004).
[21] F. Montial and M. Neviere, J. Opt. Soc. Am. A **12**, 2672 (1995).

射 频 和 天 线 设 计 培 训 课 程 推 荐

易迪拓培训(www.edatop.com)由数名来自于研发第一线的资深工程师发起成立，致力并专注于微波、射频、天线设计研发人才的培养；我们于 2006 年整合合并微波 EDA 网(www.mweda.com)，现已发展成为国内最大的微波射频和天线设计人才培养基地，成功推出多套微波射频以及天线设计经典培训课程和 ADS、HFSS 等专业软件使用培训课程，广受客户好评；并先后与人民邮电出版社、电子工业出版社合作出版了多本专业图书，帮助数万名工程师提升了专业技术能力。客户遍布中兴通讯、研通高频、埃威航电、国人通信等多家国内知名公司，以及台湾工业技术研究院、永业科技、全一电子等多家台湾地区企业。

易迪拓培训课程列表：http://www.edatop.com/peixun/rfe/129.html

射频工程师养成培训课程套装

该套装精选了射频专业基础培训课程、射频仿真设计培训课程和射频电路测量培训课程三个类别共 30 门视频培训课程和 3 本图书教材；旨在引领学员全面学习一个射频工程师需要熟悉、理解和掌握的专业知识和研发设计能力。通过套装的学习，能够让学员完全达到和胜任一个合格的射频工程师的要求…

课程网址：http://www.edatop.com/peixun/rfe/110.html

ADS 学习培训课程套装

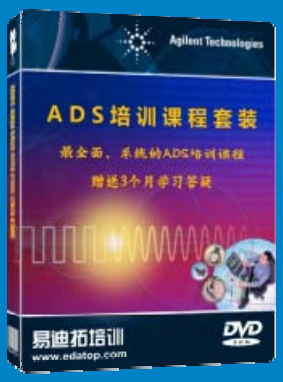

该套装是迄今国内最全面、最权威的 ADS 培训教程，共包含 10 门 ADS 学习培训课程。课程是由具有多年 ADS 使用经验的微波射频与通信系统设计领域资深专家讲解，并多结合设计实例，由浅入深、详细而又全面地讲解了 ADS 在微波射频电路设计、通信系统设计和电磁仿真设计方面的内容。能让您在最短的时间内学会使用 ADS，迅速提升个人技术能力，把 ADS 真正应用到实际研发工作中去，成为 ADS 设计专家...

课程网址： http://www.edatop.com/peixun/ads/13.html

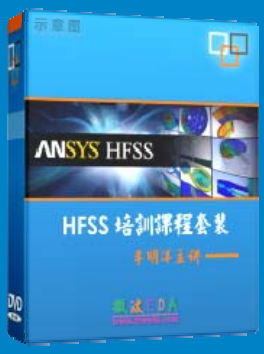

HFSS 学习培训课程套装

该套课程套装包含了本站全部 HFSS 培训课程，是迄今国内最全面、最专业的 HFSS 培训教程套装，可以帮助您从零开始，全面深入学习 HFSS 的各项功能和在多个方面的工程应用。购买套装，更可超值赠送 3 个月免费学习答疑，随时解答您学习过程中遇到的棘手问题，让您的 HFSS 学习更加轻松顺畅…

课程网址：http://www.edatop.com/peixun/hfss/11.html

CST 学习培训课程套装

该培训套装由易迪拓培训联合微波 EDA 网共同推出，是最全面、系统、专业的 CST 微波工作室培训课程套装，所有课程都由经验丰富的专家授课，视频教学，可以帮助您从零开始，全面系统地学习 CST 微波工作的各项功能及其在微波射频、天线设计等领域的设计应用。且购买该套装，还可超值赠送 3 个月免费学习答疑…

课程网址：http://www.edatop.com/peixun/cst/24.html

HFSS 天线设计培训课程套装

套装包含 6 门视频课程和 1 本图书，课程从基础讲起，内容由浅入深，理论介绍和实际操作讲解相结合，全面系统的讲解了 HFSS 天线设计的全过程。是国内最全面、最专业的 HFSS 天线设计课程，可以帮助您快速学习掌握如何使用 HFSS 设计天线，让天线设计不再难…

课程网址：http://www.edatop.com/peixun/hfss/122.html

13.56MHz NFC/RFID 线圈天线设计培训课程套装

套装包含 4 门视频培训课程，培训将 13.56MHz 线圈天线设计原理和仿真设计实践相结合，全面系统地讲解了 13.56MHz 线圈天线的工作原理、设计方法、设计考量以及使用 HFSS 和 CST 仿真分析线圈天线的具体操作，同时还介绍了 13.56MHz 线圈天线匹配电路的设计和调试。通过该套课程的学习，可以帮助您快速学习掌握 13.56MHz 线圈天线及其匹配电路的原理、设计和调试…

详情浏览：http://www.edatop.com/peixun/antenna/116.html

我们的课程优势：

※ 成立于 2004 年，10 多年丰富的行业经验，

※ 一直致力并专注于微波射频和天线设计工程师的培养，更了解该行业对人才的要求

※ 经验丰富的一线资深工程师讲授，结合实际工程案例，直观、实用、易学

联系我们：

※ 易迪拓培训官网：http://www.edatop.com

※ 微波 EDA 网：http://www.mweda.com

※ 官方淘宝店：http://shop36920890.taobao.com